Journal of Materials Chemistry A



PAPER

View Article Online
View Journal | View Issue



Cite this: J. Mater. Chem. A, 2018, 6, 17559

nanostructured Mg₂Si-Mg₂Sn solid solutions

Strain-induced suppression of the miscibility gap in

Su-in Yi,†^a Vahid Attari, (10)†^b Myunghwan Jeong, (10)^a Jie Jian,^c Sichuang Xue,^c Haiyan Wang, (10)^c Raymundo Arroyave (10)*^b and Choongho Yu (10)*^{ab}

Solid solutions of Mg₂Si and Mg₂Sn are promising thermoelectric materials owing to their high thermoelectric figures-of-merit and non-toxicity, but they may undergo phase separation under thermal cycling due to the presence of miscibility gaps, implying that the thermoelectric properties could be significantly degraded during thermoelectric device operation. Herein, this study investigates the straininduced suppression of the miscibility gap in solid solutions of Mg₂Si and Mg₂Sn. Separately prepared Mq_2Si and Mg_2Sn powders were made into $(Mg_2Si)_{0.7}(Mg_2Sn)_{0.3}$ mixtures using a high energy ball-milling method followed by spark plasma sintering. Afterwards, the phase evolution of the mixtures, depending on thermal annealing and mixing conditions, was studied experimentally and theoretically. Transmission electron microscopy and X-ray diffraction results show that, despite the presence of a miscibility gap in the pseudo-binary phase diagram, the initial mixture of Mg₂Si and Mg₂Sn evolved towards a solid solution state after annealing for 3 hours at 720 °C. Thermodynamic analysis as well as phase-field microstructure simulations show that the strain energy due to the coherent spinodal effect suppresses the chemical spinodal entirely and prevents phase separation. This strategy to suppress the miscibility gap induced by lattice strain through non-equilibrium processing can benefit the thermoelectric figureof-merit by maximizing phonon alloy scattering. Furthermore, stable solid solutions by engineering phase diagrams have the potential to facilitate the reliable long term operation of thermoelectric generators under continuous thermal loads.

Received 18th June 2018 Accepted 17th August 2018

DOI: 10.1039/c8ta05798b

rsc.li/materials-a

Introduction

Thermoelectric power generation is unique in generating electricity by utilizing low-grade heat that is typically wasted or dissipated into the environment. There has been remarkable progress in improving the performance and diversity of thermoelectric materials over the past decade. Hagnesium silicide 1-23 is an emerging thermoelectric material owing to its low density, non-toxicity, abundant raw materials, and affordable cost in contrast to conventional materials containing lead and tellurium. Recently it was reported that the thermoelectric performance of magnesium silicide can be remarkably improved when silicon is partially substituted by tin or/and germanium.

This alloyed structure induces not only phonon scattering that suppresses thermal conductivity,^{5,24–27} but also reduces the energy level differences between valleys in the electronic structures,⁶⁻⁸ increasing the power factor (PF), $S^2\sigma$, where S and σ are

the thermopower (or the Seebeck coefficient) and electrical conductivity, respectively. Therefore, the thermoelectric performance, which is typically indicated by the thermoelectric figure-of-merit, $ZT = S^2 \sigma T/k$, where T is the absolute temperature and k is the thermal conductivity, can be significantly improved. This enhancement is beyond the well-known rule of mixture explanation for composite materials.²⁸

The necessary condition to maximize ZT improvement by the alloying is to ensure the homogeneous distributions of Si and Sn (or/and Ge) in the lattice to a level such that phonons as heat carriers and electrons as charge carriers can sense the mixed elements within the range of their characteristic lengths, mean free paths and wavelengths. Hence, it is important to have a homogeneous solid solution of Mg₂Si and Mg₂Sn (or/and Mg₂Ge) during the material synthesis processes. This ideal situation has often been hard to achieve in Mg₂(Si,Sn,Ge) particularly when individual precursor powders were simply mixed for solid-state reactions. Under these processing conditions, compositional heterogeneities are typically inevitable unless large amounts of time and efforts are devoted to material synthesis.

More importantly, Si and Sn in the Si/Sn sublattice of the Mg₂Si/Sn crystal structure have a positive heat of mixing, which leads to immiscibility within the Sn/Si lattice over the entire

^aDepartment of Mechanical Engineering, Texas A&M University, College Station, TX 77843, USA. E-mail: chyu@tamu.edu

^bDepartment of Materials Science and Engineering, Texas A&M University, College Station, TX 77843, USA. E-mail: rarroyave@tamu.edu

^{&#}x27;School of Materials Engineering, Purdue University, West Lafayette, IN 47907, USA † Equally contributed to this work.

temperature range in which the mixture exists in the solid state. $^{5,9-11,29}$ The tendency towards phase separation as well as differences in the processing history of $\mathrm{Mg_2Si_xSn_{1-x}}$ mixtures may be the underlying causes for variations in the reported peak ZT values of $\mathrm{Mg_2Si_xSn_{1-x}}$, ranging mostly from 0.8 to 1.3, but this issue remains poorly studied to date. Furthermore, the miscibility gap suggests that $\mathrm{Mg_2(Si,Sn)}$ can undergo phase separation under repeated heat cycles during operation. For stable operation without significant performance degradation, it is important to suppress the miscibility gap in order to avoid phase separation.

Here we focus on elastochemical effects and the subsequent morphology changes when the mixing and annealing conditions of Si-rich and Sn-rich phases are varied. It was found that elastic energies such as elastic strains at interfaces between two phases, local lattice distortions and crystal twinning could affect microstructure evolution. To provide lattice strain, high energy ball milling and spark plasma (or current-assisted pressure) sintering (SPS) methods were employed. Unlike conventional synthesis methods, both processes have distinct characteristics of high mechanical pressure and short reaction time, which could result in significant strains between grains in polycrystalline materials.

In order to carry out the systematic study described in this work, Mg_2Si and Mg_2Sn powders were prepared separately, and then they were mixed for different time periods with high energy ball milling followed by thermal annealing. The microstructure evolution was observed experimentally and also computed theoretically. We chose a 7:3 ratio of Mg_2Si and Mg_2Sn because this composition is located well within the miscibility gap in the $Mg_2Si_xSn_{1-x}$ system, at the processing temperature, as reported in various studies – we here note that there is still considerable uncertainty regarding the location of the miscibility gap in the system. The influence of the phase separation on thermoelectric properties was experimentally measured and compared.

Experimental and simulation methods

Material synthesis

We prepared Mg₂Si powder (P168 in Table 1) and Mg₂Sn powder (P159 in Table 1) doped with 1.5 at% bismuth for the optimum thermoelectric performance²⁰ by high energy ball milling (Spex SamplePrep 8000M) with Mg turnings (99.9%, Across organics),

Si powder (99.999%, -100 + 325 mesh), Sn powder (99.8%, -325 mesh, Alfa Aesar), and Bi powder (99.9%, Strem chemicals) using 3 stainless steel balls (0.5 inch in diameter) in a stainless steel container for 10 hours at 1725 rpm (Fig. 1). After the ball milling was done separately for Mg₂Si and Mg₂Sn, X-ray diffraction (XRD) with a Bruker-AXS D8 advanced Bragg-Brentano X-ray powder diffractometer was carried out on the powders, as shown in Fig. 2a. The majority of the powders was found to be Mg₂Si or Mg₂Sn with some impurities of residual Mg, Si, and/or Sn. The powders (0.38 g for Mg₂Si and 0.6 g for Mg₂Sn) were sintered at 750 °C (Mg₂Si) or 600 °C (Mg₂Sn) for 200 seconds using SPS to make 1/2-inch diameter pellets whose density is higher than 93.5% of the theoretical density (2.0 g cm⁻³ or 3.59 g cm⁻³ respectively for Mg₂Si and Mg₂Sn). The Mg₂Si and Mg₂Sn pellets after SPS showed sharp XRD peaks without noticeable impurity peaks. The electronic mobility of these samples at room temperature ranging from 40 to 100 cm² V⁻¹ s⁻¹ from the Hall measurements was close to literature values, 20,36 suggesting that defects at grain boundaries are not significant.

The Mg₂Si and Mg₂Sn powders were mixed to have a mixture of $(Mg_2Si)_{0.7}(Mg_2Sn)_{0.3}$. This composition is within the miscibility gaps at our processing temperature no matter which of the Mg₂Sn–Mg₂Si assessed pseudo-binary phase diagrams in the literature is considered. ^{26,37,38} Therefore, this composition would give us clearer ideas if the two phases are separated or not due to the miscibility gap. According to the phase diagram, two distinct phases are supposed to appear as the samples are annealed. A mixture of Mg₂Si and Mg₂Sn powders (~2 g) was homogenized using the high energy ball miller for 0.1, 2, and 4 min. Then the mixed powders (0.46 g) were sintered using SPS at ~720 °C for 200 seconds. Finally, the samples were annealed at 720 °C for 3 and 7 hours in a sealed graphite die under a vacuum environment (<10⁻⁴ bar) to observe the evolution of the two phases, Mg₂Si and Mg₂Sn.

Thermoelectric property characterization

The synthesized pellet was polished with sand papers in order to make both faces flat and shiny. The thermal conductivity (k) was obtained by measuring the thermal diffusivity (D) with a Xeflash apparatus (TA instrument FL3000) since $k=D\rho c_{\rm p}$, where ρ is the density measured using the Archimedes method, and $c_{\rm p}$ is the specific heat^{29,36,39} from the literature. For the measurement

Table 1 List of samples $(Mg_2Si)_x(Mg_2Sn)_{1-x}$ experimentally tested for this study along with their synthesis conditions and electrical properties at room temperature

Sample #	x	Ball milling time (min)	Post annealing time (hour)	Density (%)	Electrical conductivity (S cm ⁻¹)	Carrier concentration $(10^{20} \text{ cm}^{-3})$	Mobility $(cm^2 V^{-1} s^{-1})$
P168	1.0	N/A	0	99.5	1270	1.9	41
P169	0.7	0.1	0	102	1790	2.2	50
P172		2	0	102	1510	2.3	41
P174		4	0	102	1420	2.1	42
P170		2	3	96	1620	1.9	53
P173		4	7	97	1870	2.8	42
P159	0.0	N/A	0	93.5	3730	2.3	100

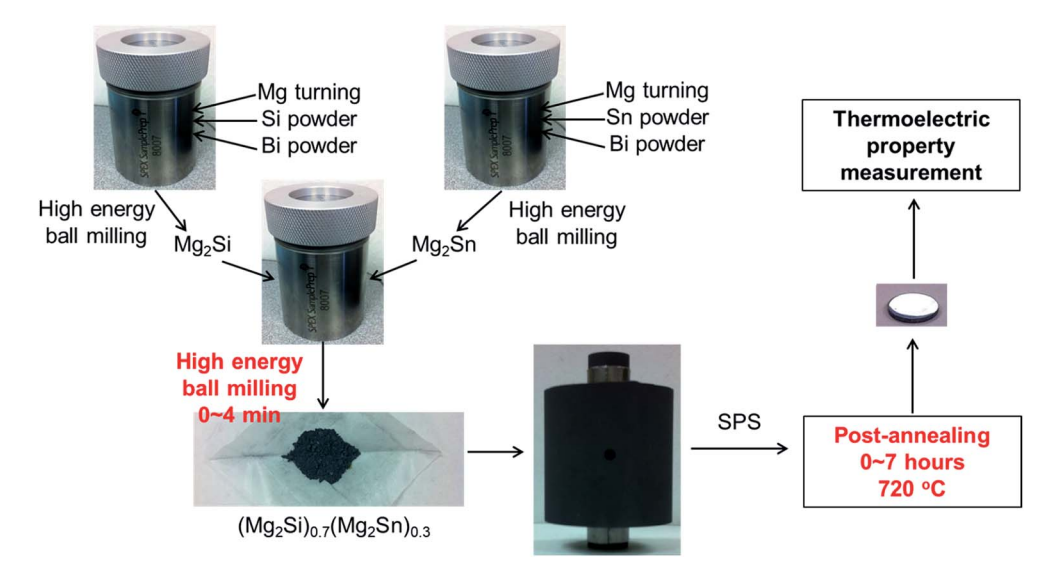


Fig. 1 Material preparation procedures and subsequent thermal annealing and measurements.

of thermopower and electrical conductivity, the pellets were cut into a bar whose dimension is $1.3\times5\times11~\mathrm{mm}^3$ using a diamond saw, and then mounted in our custom-built setup. The electrical conductivity was obtained from the slope of voltage as a function of supplied current ranging from $-0.05~\mathrm{A}$ to $0.05~\mathrm{A}$ and the geometry of the samples. The thermopower was obtained from the slope of voltage with respect to the temperature difference ranging from $-15~\mathrm{K}$ to $15~\mathrm{K}$. Hall measurements were carried out using a custom-built setup under a 1T magnetic field at room temperature.

Phase field approach

The total free energy functional (F^{tot}) for an undeformed material configuration with confined boundaries can be constructed from the sum of all contributing fields over it. F^{tot} can be a functional of composition (c), strain (ϵ), gradients of composition (∇c), and other fields if present. We write the total free energy functional, F^{tot} as the sum of contributing fields:

$$F^{\text{tot}}(c, \varepsilon, \nabla c) = f^{\text{chem}} + f^{\text{elas}}$$
 (1)

where the chemical free energy density, $f^{\rm chem}$, and elastic strain energy density, $f^{\rm elas}$ are:

$$f^{\text{chem}}(c, \nabla c) = \int_{\Omega} \left[\varkappa(\nabla c)^2 + f^{\text{bulk}}(c) \right] d\Omega$$
 (2)

$$f^{\text{elas}}(\varepsilon) = \frac{1}{2} \int_{\Omega} \varepsilon^{\text{el}} \sigma^{\text{el}} d\Omega$$
 (3)

where \varkappa is the gradient energy coefficient, and f^{bulk} is the contribution of the bulk phases in the microstructure. ε^{el} and σ^{el} are the local elastic strain and stress in the material. The chemical free energy is composed of the interfacial and bulk energy contributions, and it determines the compositions and volume fractions of the equilibrium phases. The strain energy affects the equilibrium compositions and volume fractions of the coexisting phases, but also determines the shapes and

configurations of the phase domains. In an inhomogeneous solid solution, the generalized potential for phase transformation, μ^{tot} , as a function of the concentration, the deviations in concentration, and the elastic strain can be calculated by means of the given free energy functional in eqn (1) as:

$$\mu^{\rm tot}(c, \varepsilon, \nabla c) = \frac{\delta F^{\rm tot}}{\delta c} = \frac{\partial F^{\rm tot}}{\partial c} - \nabla \left(\frac{\partial F^{\rm tot}}{\partial \nabla c}\right) \tag{4}$$

$$\mu^{\text{tot}} = \frac{\partial f}{\partial c} - \nabla(\varkappa \nabla c) + \nabla c \frac{\partial \varkappa}{\partial c} \nabla c - 2\nabla \varepsilon^{0}(c) : C(c)(\varepsilon^{\text{el}}) + (\varepsilon^{\text{el}} : \nabla C(c)(\varepsilon^{\text{el}}))$$
 (5)

The separation process of two distinct phases from a homogeneous solution due to small fluctuations in the composition is the case where the system is unstable, and the chemical potential is the main responsible driving force for this uphill diffusion process leading to phase separation, while the strain energy acts in the reverse way to mitigate the phase separation most of the time. From the linear kinetic theory, the local mass flux in the presence of a gradient in composition, the diffusion flux (in units of mol m^{-2} s⁻¹) is given by:

$$\vec{J} = -\vec{M}\nabla\mu^{\text{tot}} = -\vec{M}\nabla\left(\frac{\delta F^{\text{tot}}}{\delta c}\right) \tag{6}$$

where \vec{M} is the interface mobility assumed to be constant due to the isotropic nature of the crystal structures of the two phases. We postulate the following form of the Cahn–Hilliard (C–H) kinetic equation to study the evolution of the Mg₂Si–Mg₂Sn microstructure in a 2-dimensional (2D), and 3-dimensional (3D) space:

$$\frac{\partial c}{\partial t} = \nabla \vec{M} \nabla (\mu^{\text{tot}}) \tag{7}$$

Given an initial microstructure, the evolution of the microstructure can be studied by solving the Cahn-Hilliard equation

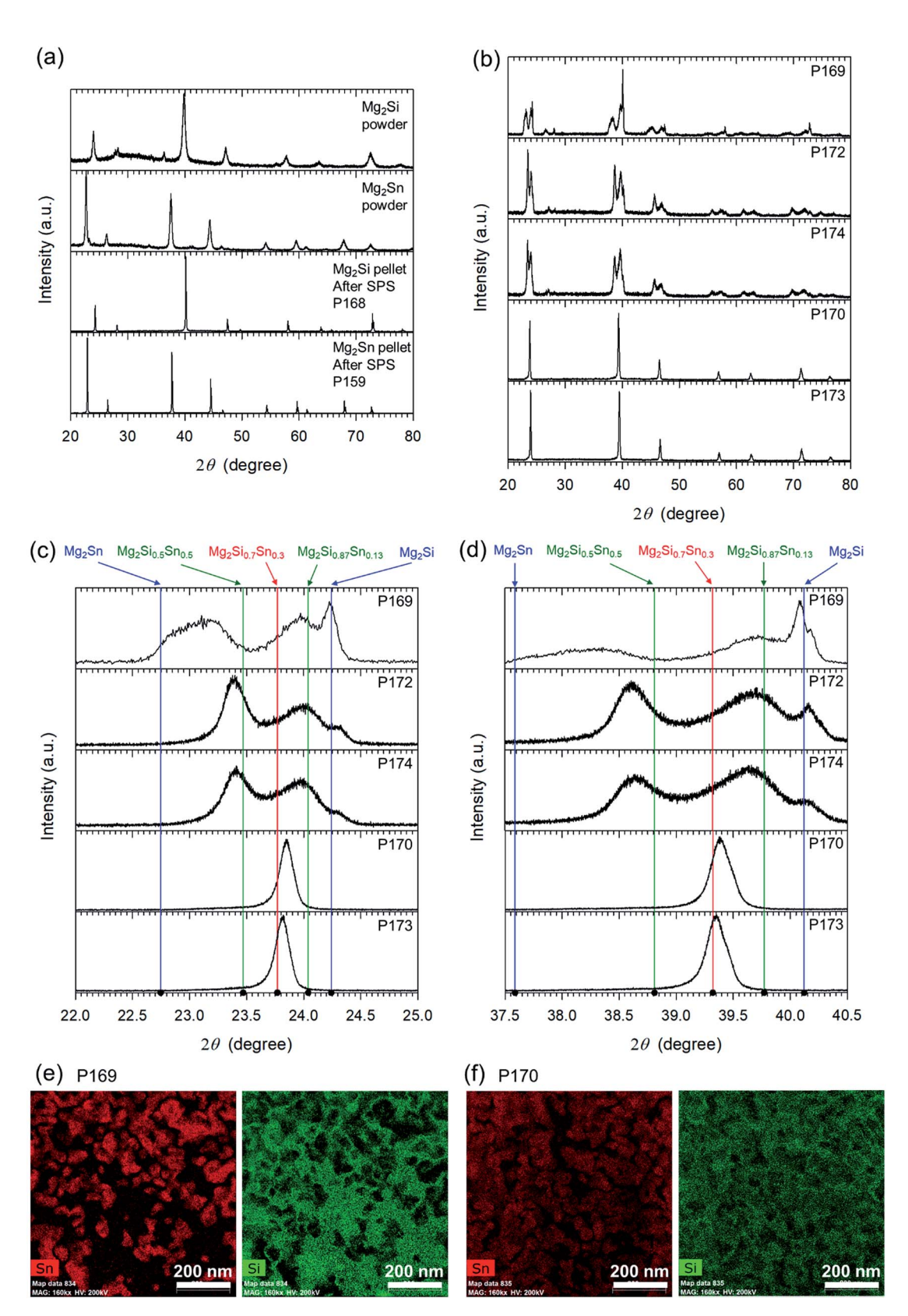


Fig. 2 XRD results of (a) synthesized Mg_2Si and Mg_2Sn powders and pellets after SPS; (b) mixtures of Mg_2Si and Mg_2Sn in Table 1. Detailed analyses of the XRD results near (c) (111) and (d) (220) planes. Five vertical lines correspond to the peak locations for various Si: Sn ratios: Mg_2Sn , $Mg_2Si_{0.5}Sn_{0.5}$, $Mg_2Si_{0.7}Sn_{0.3}$, $Mg_2Si_{0.87}Sn_{0.13}$, and Mg_2Si . EDS results of (e) P169 and (f) P170.

using a semi-implicit spectral approach in the Fourier space. The elastic energy contribution to the kinetics of evolution is obtained using the microelasticity theory. 40,41 There are three factors contributing to the elastic potential: (1) the lattice misfit between the different phases, (2) the elastic constant inhomogeneity, and (3) externally applied stress. In this study, no external force is applied. The microelasticity problem is posed

$$\frac{\partial \sigma_{ij}}{\partial r_i} = 0 \text{ in } \Omega \tag{8}$$

$$\varepsilon_{kl} = \frac{1}{2} \left\{ \frac{\partial u_k}{\partial r_l} + \frac{\partial u_l}{\partial r_k} \right\} \tag{9}$$

$$\sigma_{ii}^{\text{el}} = C_{iikl} \varepsilon_{kl}^{\text{el}} \text{ where } \varepsilon_{kl}^{\text{el}} = \varepsilon_{kl}^{\text{tot}} - \varepsilon_{kl}^{0}$$
 (10)

Eqn (8), (9), (10) are the mechanical equilibrium condition, kinematics, and Hook's microscopic constitutive law for linear elasticity, respectively. $\varepsilon_{kl}^{\rm el}$ is the difference between the total strain $\varepsilon_{kl}^{\text{tot}}$ and the eigenstrain ε_{kl}^{0} . The dilatational eigenstrain term is $\varepsilon_{kl}^0 = \varepsilon^T \delta_{kl} h(c)$, and it is the consequence of lattice strain between the phases. The lattice misfit is $\varepsilon^T = (a^{\alpha} - a^{\beta})$ $0.5(a^{\alpha} + a^{\beta})$ where a^{α} and a^{β} are the lattice parameters of α and β phases, respectively. δ_{kl} is the Kronecker-delta function and h(c) is an interpolation function. C_{ijkl} is the compositiondependent fourth order elastic modulus tensor. It is convenient to describe C_{ijkl} using the following expression:

$$C_{ijkl}(c) = C_{ijkl}^{\text{eff}} - g(c)\Delta C_{ijkl}$$
 (11)

where $\Delta C_{ijkl} = C^{\alpha}_{ijkl} - C^{\beta}_{ijkl}$ is the difference between the elastic moduli tensor of α and β phases. Similar to h(c), g(c) is a scalar interpolation function such that $h(c_{\alpha}) = g(c_{\alpha}) = 0$ and $h(c_{\beta}) =$ $g(c_B) = 1$. Having a periodic boundary condition, the higherorder solutions for the system of eqn (8)-(10) are obtained in the Fourier space based on the lower-order approximations in an iterative manner. A semi-implicit Fourier spectral approach⁴² for the C-H equation is used.

Results and discussion

X-ray diffraction and energy dispersive spectroscopy analysis

P169, P172, P174, P170, and P173 in Table 1 show a list of samples prepared by mixing Mg2Si and Mg2Sn powders with a molar ratio of 7:3. According to a recent paper, 26 this composition is placed at the center of the miscibility gap in the Mg₂Si-Mg₂Sn binary material system so equal amounts of separated phases, Mg₂Si_{0.5}Sn_{0.5} and Mg₂Si_{0.87}Sn_{0.13}, are expected to be obtained as they go through mixing and thermal processing at \sim 720 °C. XRD results in Fig. 2b show phase evolution as the mixture of Mg₂Si and Mg₂Sn went through longer high energy ball milling and thermal annealing.

Surprisingly, as shown in Fig. 2b, the peak pairs (the same crystal plane) from Si-rich and Sn-rich Mg₂Si₂Sn_{1-r} were merged with longer mixing and annealing, which is opposite to what the phase diagrams in the literature describe. We carried

out detailed analysis near the major two peak locations (111) in Fig. 2c and (220) in Fig. 2d. Sample P169 with short 0.1 min mixing showed distinct two peaks from Sn-rich and Si-rich phases. In Fig. 2c, we noticed that the (111) peak from the Sirich phase at 24.23° is close to 24.241° from JCPDS 00-035-0773 for Mg₂Si and has a relatively narrow full width at half maximum (FWHM), but the (220) peak at \sim 23.1° from the Snrich phase is broad, and shifted toward a higher angle compared to 22.747° from JCPDS 00-007-0274 for Mg₂Sn. Another peak at $\sim 24.0^{\circ}$ in the middle was also found, suggesting that some of the two phases were miscible. The shifted, broad peak corresponding to Sn-rich phase is likely to indicate that the Sn-rich phase was strained by the Si-rich phase. Considering the lower melting point of Mg₂Sn (778 °C) compared to Mg₂Si (\sim 1085 °C) (SPS temperature, 720 °C), it is probable that softened Mg₂Sn was smeared into spaces between Mg₂Si particles, forming separated Mg₂Si and Mg₂Sn islands as shown in the energy dispersive spectroscopy (EDS) results (Fig. 2e).

When the ball milling time was increased to 2 min (P172) and 4 min (P174), the Si-rich peak at ~24.23° was suppressed and the Sn-rich peak became sharper and further shifted, showing two prominent peaks at $\sim 23.4^{\circ}$ and $\sim 24.0^{\circ}$, which are close to the precipitating phases (~23.47° for Mg₂Si_{0.5}Sn_{0.5} and $\sim 24.04^{\circ}$ for Mg₂Si_{0.87}Sn_{0.13}) according to the miscibility gap of the phase diagrams reported in the literature. However, when the samples were annealed for 3 hours (P170) and 7 hours (P173), the two peaks were merged toward the theoretically calculated peak position at 23.47° for Mg₂Si_{0.7}Sn_{0.3}, suggesting the suppression of the miscibility gap. Similar trends were observed from the (220) plane (Fig. 2d). According to JCPDS, corresponding angles are 37.587° and 40.121° for Mg₂Sn and Mg₂Si, respectively. Two broad peaks close to the two precipitating phases (38.81° for Mg₂Si_{0.5}Sn_{0.5} and 39.77° for Mg₂-Si_{0.87}Sn_{0.13}) were found from P172 and P174, and then, after thermal annealing, they were merged into a single peak, which is close to 29.32° for Mg₂Si_{0.7}Sn_{0.3}. Note that the peak angle locations for the solid solutions (Mg₂Si_{0.5}Sn_{0.5}, Mg₂Si_{0.7}Sn_{0.3}, Mg₂Si_{0.87}Sn_{0.13}) were calculated from the lattice constants obtained by interpolation with the lattice constants of Mg₂Si and Mg₂Sn.

The EDS results (Fig. 2e) from Sample P169 showed segregated Sn-rich and Si-rich phases, whose dimensions are less than 100 nm. On the other hand, the EDS results in Fig. 2f for Sample P170 with 3 hours annealing displayed dull colors with smaller reddish and greenish regions, suggesting a much better degree of mixing although relatively richer Si and Sn regions are observable. Nevertheless, despite the presence of varying compositions according to the EDS results, the XRD results for P170 show merged peaks corresponding to a homogeneous solid solution. In fact, similar results are also displayed in other papers. 9,29 Therefore we can conjecture that the small grains are strained. To maintain the strain, coherent boundaries may be present like in other samples prepared similarly using ball milling and SPS processes.36

Phase stability analysis in the Mg_2Si-Mg_2Sn pseudo-binary system

Our XRD and EDS results indicate that Mg_2Si and Mg_2Sn are miscible in the composition and the processing temperature ($X_{Si} = 0.7$ at 720 °C) in this study. A close look at the available pseudo-binary phase diagram of the Mg_2Sn-Mg_2Si system suggests that there are considerable uncertainties in the location of the Sn-rich and Si-rich phase boundaries in the Mg_2Sn-Mg_2Si pseudo-binary system, as shown in Fig. 3a. Except for the

study by Nikitin *et al.*,⁴³ other experimental and theoretical assessments^{26,37,38,44,45} show that the selected composition and temperature are located well within the chemical miscibility region of the phase diagram, as discussed below.

Considering the location of the Sn-rich phase boundary in the Mg_2Sn-Mg_2Si pseudo-binary system, all experimental evidence presented to date suggests that this boundary is located within the $0.1 < X_{Si} < 0.45$ range near our processing temperature. Over a wide temperature range, Muntyanu *et al.*,⁴⁴

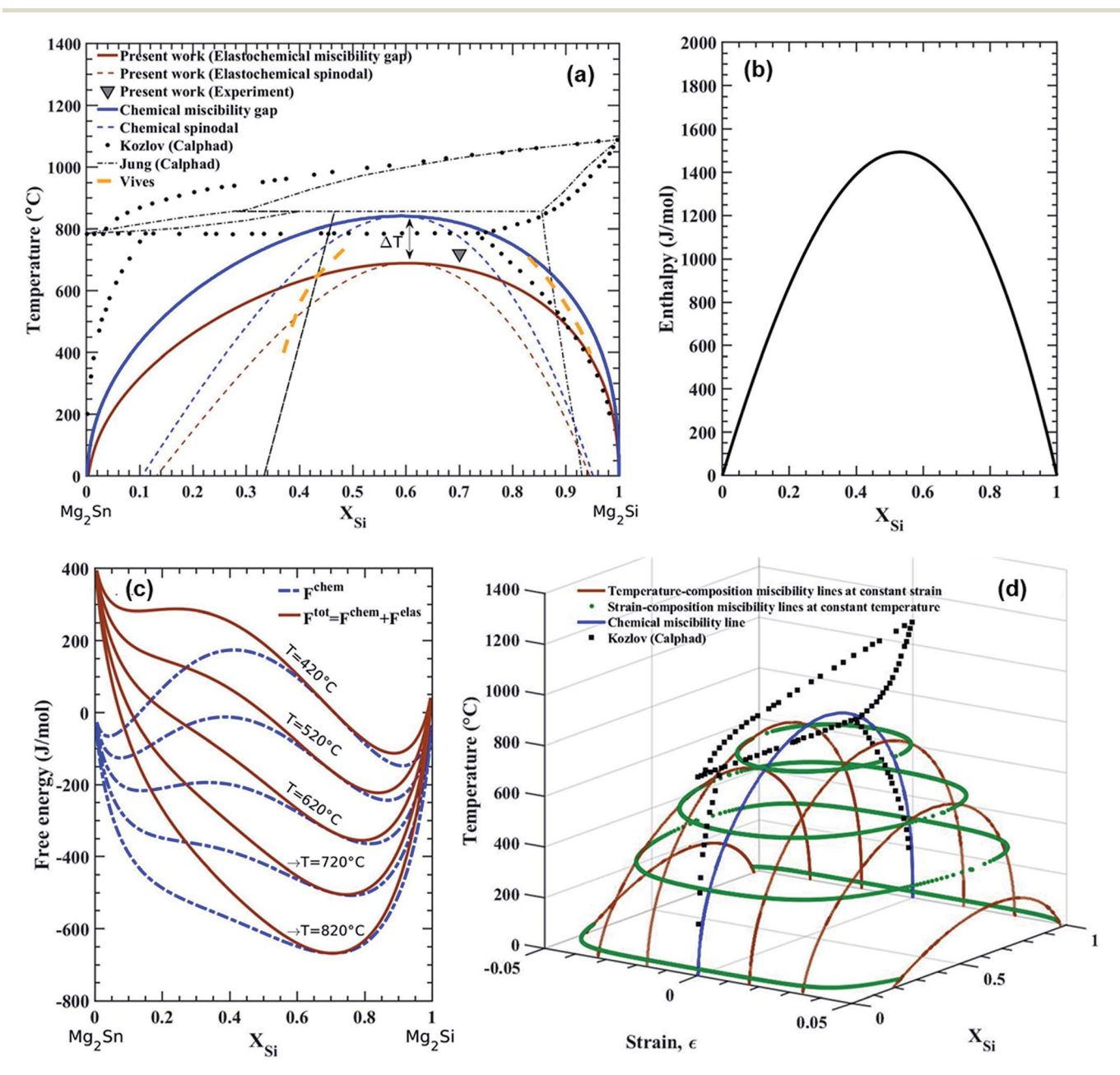


Fig. 3 (a) Calculated elastochemical miscibility gap *versus* the chemical gap showing the shift of the miscibility gap and spinodal lines due to the strain energy impact. Experimental data are taken from the literature. The parameters used in calculation of the elastochemical miscibility gap are summarized in Table 2. (b) Enthalpy of formation. (c) Total elastochemical energy curves *versus* chemical energies at 420 °C, 520 °C, 620 °C, 720 °C, and 820 °C. (d) The three-dimensional strain-composition-temperature phase diagram for the Mg₂Si-Mg₂Sn pseudo-binary system. The red and green lines are elastochemical miscibility lines whereas the blue lines are chemical miscibility lines. For comparison, the miscibility gap from Kozlov *et al.* is plotted.

Nikitin et al.,43 and Jung et al.45 show that this boundary is within the 0.35 $< X_{Si} < 0.45$ range. Kozlov et al.³⁷ carried out experimental investigations on this system and performed an assessment of its phase stability based on their own data as well as any other existing phase stability information published prior to their work. Their assessed pseudo-binary phase diagram indicates that the phase boundary is around $X_{\rm Si} \sim 0.1$ at our processing temperature. In a later assessment by Viennois et al., 38 this phase boundary is located at $X_{\rm Si} \sim 0.3$, somewhat in between the analysis by Kozlov and Nikitin/Jung. The most recent investigation on the phase stability of this system was carried out by Vivès et al.,26 who performed diffusion couple experiments over a wide range of temperatures and identified X_{Si} ~ 0.4 as the location of the Sn-rich phase boundary in the Mg₂Sn-Mg₂Si miscibility gap. While there is evidently considerable uncertainty as to the exact location of this phase boundary, the composition used in this study, $X_{Si} = 0.7$, is clearly to the right of all assessed solubility limits for Si in Mg₂Sn.

When looking at the Si-rich phase boundary, we would like to note that every single investigation of the system, except for Nikitin $et~al.^{43}$ indicates that the alloy investigated in this work is to the left of the Si-rich phase boundary (Sn solubility limit for Mg₂Si). This phase boundary is located around $X_{\rm Si}\sim 0.9$ in the study by Muntanyu $et~al.,^{44}$ Jung $et~al.,^{45}$ Viennois $et~al.,^{38}$ and Vivès $et~al.,^{26}$ and Kozlov $et~al.,^{37}$ locate this boundary at slightly lower values of Si, $X_{\rm Si}\sim 0.78$. Out of all the existing evidence, only the assessed Si-rich phase boundary by Nikitin et~al. places our alloy outside the miscibility gap (to the right of the Si-rich phase boundary).

A thorough analysis of this apparent inconsistency was carried out by Kozlov $et\,al.$, who compared their own differential scanning calorimetry and thermal analysis for different alloys as well as the phase constitution and composition of solidified alloys belonging to this system and conclusively showed that the phase boundary reported by Nikitin $et\,al.$ could not be reconciled with available data. Perhaps an even stronger piece of evidence that puts into question the results by Nikitin $et\,al.$ is the diffusion couple study by Vivès $et\,al.$ which suggests that the phase boundary is closer to $X_{\rm Si}\sim 0.9$, in agreement with five decades worth of research on this system and in contradiction with Nikitin $et\,al.$ Given the preponderance of evidence, we are confident that the alloy investigated in this work is well within the Mg₂Sn–Mg₂Si bulk chemical miscibility gap.

In the present study, however, under the non-equilibrium synthesis conditions, it is not clear that the system phase separates in the composition ($X_{\rm Si}=0.7$) well within the miscibility gap. Here we investigate the possible underlying reasons for this observation from a thermodynamic perspective using eqn (1). We use the pseudo-binary phase diagram obtained by Viennois *et al.* ³⁸ Assuming ideal entropy of mixing, Viennois *et al.* proposed the following equation for calculating the mixing Gibbs energy, $\Delta_{\rm mix}G$:

$$\begin{split} \Delta_{\text{mix}} G\big(\text{Mg}_{2/3} \mathbf{X}_{c/3} \mathbf{Y}_{(1-c)/3}\big) &= \Delta_{\text{mix}} H\big(\text{Mg}_{2/3} \mathbf{X}_{c/3} \mathbf{Y}_{(1-c)/3}\big) \\ &+ \frac{RT}{3} (c_i \ln c_i + (1-c_i) \ln(1-c_i)) \end{split}$$
(12)

where the mixing enthalpy, $\Delta_{mix}H$ shown in Fig. 3b, was obtained using a fit of $\Delta_{mix}E$ with Redlich-Kister polynomials as in standard CALPHAD approaches and X = Si and Y = Sn in this formulation. Hence, the mixing Gibbs energy can be rewritten as:

$$\Delta_{\text{mix}} G(\text{Mg}_{2/3} X_{c/3} Y_{(1-c)/3}) = \sum_{i=1}^{n-1} \sum_{j=i+1}^{n} c_i c_j L_{ij} + \frac{RT}{3} (c_i \ln c_i + (1-c_i) \ln (1-c_i))$$
(13)

with $L_{ij} = \sum_{\nu=0}^{k} (c_i - c_j)^{\nu} L_{ij}$, where $^{\nu}L_{ij}$ is the temperature invariant interaction parameter. $c_i = c_{\rm Sn}$ and $c_j = c_{\rm Si}$. $^0L_{ij}$ and $^1L_{ij}$ are 5950 and -800 J mol $^{-1}$, respectively and the two parameters are sufficient for the parameterization of the subregular-solution model. The mixing Gibbs energies at 420, 520, 620, 720 and 820 °C are shown in Fig. 3c. A close look at the pseudo-binary free energy curves reveals that the double-well free energy and hence the miscibility gap diminishes by increasing the temperature due to the entropic stabilization, and closes at \sim 845 °C.

In addition to chemical contributions, we consider the local contractions/expansions upon phase transformation, which produce additional strain energy terms. By replacing $F^{\rm chem}$ with $\Delta_{\rm mix}G$ in eqn (10) and, following the approach proposed by Cahn,³⁰ we write the following total free energy for the material:

$$F^{\rm tot} = \Delta_{\rm mix} G \left({\rm Mg_{2/3} X_{c/3} Y_{(1-c)/3}} \right) \ + \int_{\varOmega_{\rm m}} \frac{2\alpha_c^2 E}{1-\nu} (c-c_0)^2 {\rm d} \varOmega_{\rm m} \ \ (14)$$

where the second term is the total elastic energy of an isotropic solid with arbitrary composition fluctuations. In the last term, $\Omega_{\rm m}$ is the molar volume, and α_c is Vegard's parameter ($\alpha_c = \varepsilon_{ii}{}^{\sigma=0}/\delta c$), where $\varepsilon_{ii}{}^{\sigma=0}$ is the stress-free dilatational strain. E is the Young's modulus, ν is Poisson's ratio, and c_0 denotes the overall (average) composition of the material. Fig. 3c compares the calculated elastochemical free energies with the chemical curves at different temperatures. Eventually, these calculations depict the gradual conversion of double-wells into parabolas at temperatures around \sim 680 to \sim 845 °C due to elastic interactions. These results infer that the coherency strains stabilize the material against infinitesimal composition changes in this temperature range which is in agreement with our experimental observations.

The boundaries of the elastochemical pseudo-binary miscibility gap and spinodal lines for the Mg₂Sn–Mg₂Si were calculated by linear stability analysis, as shown in Fig. 3a. In calculation of these lines we have assumed the validity of small-strain elasticity theory in an isotropic system neglecting any other change in excess thermodynamic quantities. The parameters used to obtain these curves are summarized in Table 2. The figure illustrates the experimental point in the present work and the pseudo-binary phase diagram by Kozlov *et al.*,³⁷ Jung *et al.*,⁴⁵ and Vivès *et al.*²⁶ The point that is indicated by the inverse triangle resides in the chemical spinodal region. However, it is above the obtained elastochemical miscibility gap indicating the tendency to form a solid solution under highly non-equilibrium processing conditions.

The important concepts of intrinsic stability and thermodynamics of systems under externally controlled thermodynamic

Table 2 Material properties of Mg₂Si and Mg₂Sn

		Elastic constants (GPa) ^{52,53}						
Phase	Lattice constant (nm) ⁵¹	C_{11}	C_{12}	C_{44}	Young modulus (GPa) ^{52,53}	Poisson coef.	Molar volume (m³ mol ⁻¹) ⁵⁴	Interface mobility $(m^2 s^{-1})$ [this work]
Mg ₂ Sn Mg ₂ Si	$6.327 + 6.5 \times 10^{-5}T + 4 \times 10^{-8}T^{2}$ $6.732 + 8.5 \times 10^{-5}T + 3.8 \times 10^{-8}T^{2}$	83.71 114.07	39.79 19.56	21.69 33.32	57 118	0.2058 0.1464	$1.55 \times 10^{-5} \\ 3.95 \times 10^{-5}$	$\sim \! 10^{-12}$

variables were originally coined by Gibbs, ⁴⁷ Tisza, ⁴⁸ Cahn, ⁴⁹ and Huh–Johnson. ⁵⁰ It is well established that, to have an intrinsic instability, it is necessary to have at least one negative eigenvalue for the Hessian matrix of the second derivative of the free energy functional with respect to infinitesimally small perturbations. Following the limit of metastability, we have spanned the chemical miscibility line around the strain, composition and temperature space. Fig. 3d shows the obtained three-dimensional phase diagram in the strain–composition–temperature space. The pseudo-binary phase diagram by Kozlov *et al.* ³⁷ resides at $\varepsilon = 0$, which corresponds to the bulk state. In this figure, two subsets of lines are present for constant strains and constant temperatures indicated by vertical and horizontal brown lines, respectively. The elastochemical miscibility line in Fig. 3a is a subset of this space along constant strain.

Phase field modeling of Mg₂Sn-Mg₂Si microstructural evolution

In order to further analyze this unusual observation of suppression of a solid miscibility gap, the evolution of the microstructure was investigated through phase field kinetics simulation based on the structural configuration from EDS analysis for mapping the distribution of Sn and Si atoms (Fig. 2e) (sample P169). Individual distribution information of Sn and Si atoms from EDS was post-processed so as to obtain the microscopic stoichiometry of x in $\mathrm{Mg_2Si_xSn_{1-x}}$ with a resolution of 1–2 nm. The initial microstructure for 2D simulation was obtained from the EDS data of P169. The initial condition in the 3D case is a generated synthetic microstructure based on the average grain value of $\mathrm{Mg_2Sn}$ phases from EDS data of P169.

Then, both 2D and 3D synthetic microstructures were computationally annealed for 3 hours at 720 °C. We comparatively investigated the strain effect in addition to the chemical effect. The distribution of the elastic strains (ε_{xx}^{elas} , ε_{yy}^{elas} , and ε_{xy}^{elas}), and the values along the line (*) are shown in Fig. 4. The calculations show that Mg₂Sn phases are under compressive strains. Fig. 5 compares the evolution of the microstructure for chemical only and elastochemical regimes. When only chemical interactions were considered, the microstructure followed the normal spinodal decomposition route, and the microstructure became more locally segregated and coarser over time. In this case, the gradient energy coefficient (\varkappa) controls the rate of coarsening. When we considered the strain effects in the model,

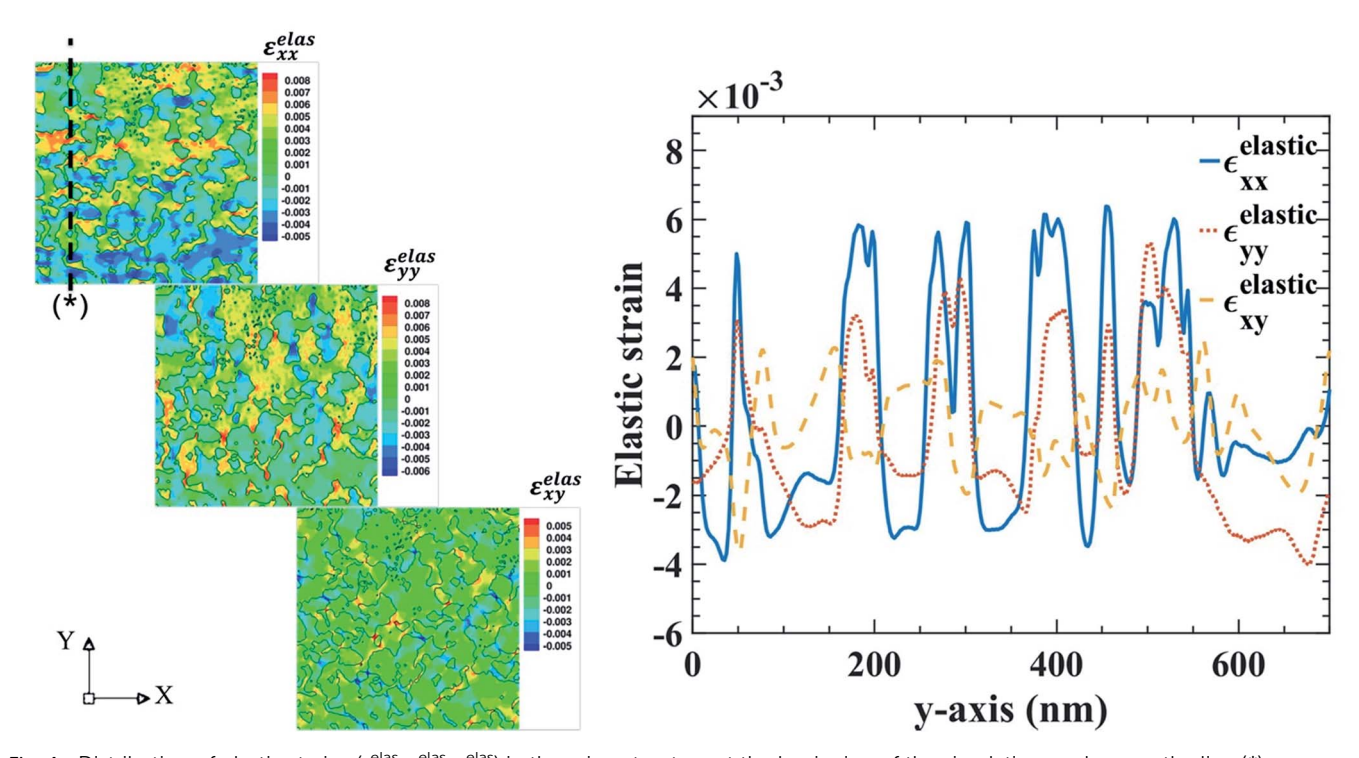


Fig. 4 Distribution of elastic strains (ε_{xx}^{elas} , ε_{yy}^{elas} , ε_{yy}^{elas}) in the microstructure at the beginning of the simulation, and across the line (*).

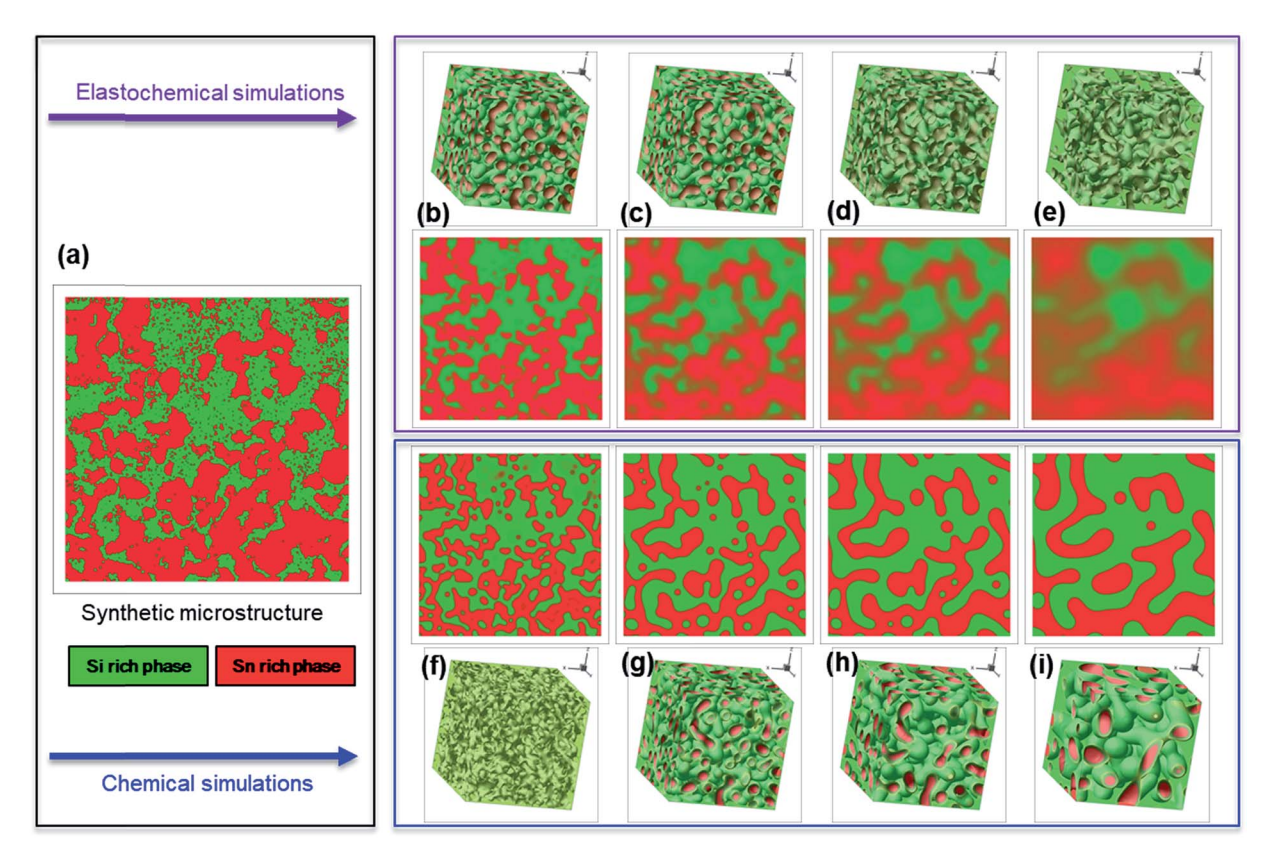


Fig. 5 Evolution of Mg₂Si-rich and Mg₂Sn-rich phases when elastochemical (top row) or chemical only (bottom row) simulations were considered. (a) Initial condition (sample 169), 2D and 3D simulation results during the 720 °C annealing process by considering elastochemical interactions after (b) 2 minutes, (c) 30 minutes, (d) 1 hour, and (e) 3 hours, and (f-i) those by considering only chemical interactions.

Mg₂Sn phases started to slowly release Sn to the Mg₂Si matrix. Eventually, the domain gets dispersed throughout with Sn and Si elements. In the end, the overall molar concentration of Si in the domain reaches 0.7 over the entire domain. The obtained semi-uniform composition of 0.7 is close to the minimum of the elastochemical free energy curve at 720 °C as depicted in Fig. 3c. Experimental EDS results in Fig. 2f (sample P170) also suggest that Si and Sn get more dispersed in the domain, and the XRD results also indicate that the two separate peaks were merged after the annealing process. We believe that the system tends to dissolve and form a solid solution, instead of following the phase separation path suggested by the metastable phase diagrams published in the literature.

By matching the simulated microstructures after the isothermal annealing treatment to the experimentally observed microstructure, the free parameters of the model (i.e., mobility and gradient energy coefficient) were estimated. In the case of coherent microstructural evolution, the interfacial mobility and the gradient energy coefficient are estimated to be around $10^{-12}~\text{m}^2~\text{s}^{-1}$ and $10^{-1}~\text{J}~\text{m}^{-2}$, respectively at 720 °C. Fig. 6 shows that the Si concentration is reduced in Mg₂Si-rich sites and is increased in Mg₂Sn-rich sites over time until it reaches an equilibrium value, which corresponds to a degree of immiscibility that is considerably smaller than what is observed in the bulks without such nanoscale crystalline grains. This figure is obtained by tracking the maximum and minimum values of concentration in the simulation cell. In fact, according to our simulations, the composition gap between Si-rich and Snrich regions of the microstructure should be no more than about 0.1 in molar concentration units. These results are consistent with the experimental observations showing that the system tends to become more homogeneous after annealing, even in samples that appear to be within the miscibility gap found in bulk phase stability studies.

The influence of phase evolution on thermoelectric transport properties

The thermal conductivities of P169, P172, P174, P170, and P173 whose x is 0.7 in $(Mg_2Si)_x (Mg_2Sn)_{1-x}$ were measured, as shown in Fig. 7a. The decreasing thermal conductivity as a function of temperature suggests negligible bipolar thermal conductivity, which implies degenerate doping as well as larger band gaps compared to that of $Mg_2Si_xSn_{1-x}$ with x = 0.3 as reported in the literature.6 It is notable that P169 with least mixing of the two phases displayed higher thermal conductivities than other samples. It is noteworthy that the thermal conductivities of P172 and P174, whose XRD peaks indicate some degrees of phase separation, are similar to those of P170 and P173 whose XRD peaks from Sn-rich and Si-rich phases were merged. This is a good indication that alloy scattering is very effective in dropping the thermal conductivity of this system, similarly to other alloys such as Si_xGe_{1-x} .

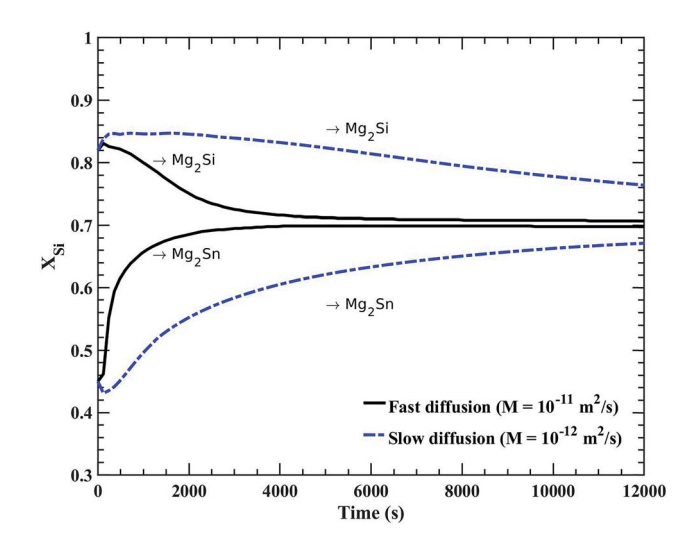


Fig. 6 Elemental dissolution from the Sn and Si lattice sites of Mg₂Sn and Mg₂Si phases toward the formation of a solid solution. Estimated dissolutions with a rate of 10^{-12} m² s⁻¹ (solid curves) and 10^{-11} m² s⁻¹ (dashed curves)

The lattice thermal conductivities of two representative samples (P169 - least mixed; P173 - most mixed) were obtained after subtracting the electronic thermal conductivity portion using the Wiedemann Franz law, as shown in Fig. 7b. The higher phase homogeneity in P173 resulted in lower thermal conductivity. The

experimental data points were fitted using the modified Callaway model for phase segregated materials.5 This model considers three simplified components, phase-pure portions (Mg₂Si, Mg₂Sn) and mixed portions (Mg2Si0.7Sn0.3). According to the fitting results, P169 has a 27% unmixed portion out of the entire volume. It should be noted that Mg₂Si_{0.7}Sn_{0.3} represents the mixed portions with various compositions (i.e., $Mg_2Si_xSn_{1-x}$ where 0 < x< 1) because even slight alloying drops the thermal conductivity to the values observed from well-mixed samples. Therefore, we could say an \sim 27% volume of P169 is composed of relatively phase-pure materials and \sim 73% volume is composed of solid solutions, Mg₂Si_xSn_{1-x} with various compositions. On the other hand, a much smaller (\sim 7%) volume of P173 was estimated to be phasepure.

Fig. 7c and d show the electrical conductivity and thermopower measurement data of the two representative samples. The carrier concentrations were measured to be 2.2×10^{20} cm⁻³ for P169 and 2.8 \times 10²⁰ cm⁻³ for P173. This suggests that most of the Bi dopant in P169 is active (Mg2Si0.985Bi0.015 and Mg₂Sn_{0.985}Bi_{0.015}). The electrical conductivity decreases with temperature, indicating the degenerate doping. The negative sign of thermopower whose magnitude is smaller than 200 μV K^{-1} also supports the fact that our samples are heavily-doped ntype semiconductors. The electrical conductivity and thermopower of P173 are similar to those of P169 despite 30% higher carrier concentration compared to P169, which may be

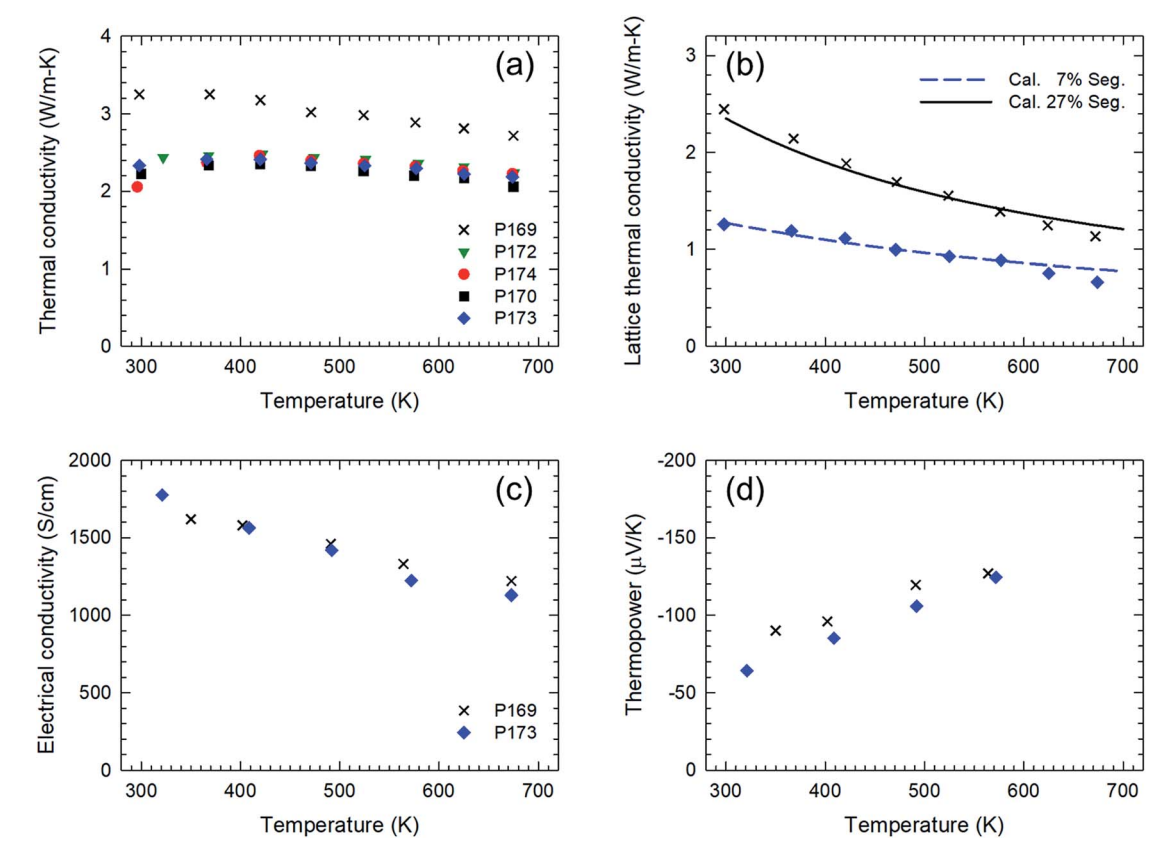


Fig. 7 (a) Thermal conductivity of samples, (b) lattice thermal conductivity with calculation results, (c) electrical conductivity, and (d) thermopower.

attributed to the more significant scattering due to alloy or/and strained grain boundaries in P173.

Conclusions

Mg₂Si and Mg₂Sn powders were separately prepared, and they were mixed for different time periods using a high energy ball miller. The mixed powders were sintered by SPS and then the sintered pellets were annealed for different time periods to evaluate the evolution of the two phases. We studied the 7:3 composition for (Mg₂Si): (Mg₂Sn), which is well within the miscibility gaps reported in the literature. According to XRD and EDS results, the two separate phases indicating Mg₂Si-rich regions and Mg₂Sn-rich regions were clearly present when the two powders were gently mixed. With more rigorous mixing, XRD results indicated that the two phases are miscible. Upon thermal annealing, XRD peaks from Mg₂Si-rich and Mg₂Sn-rich phases were merged, and EDS results also displayed a much higher degree of mixing, which is inconsistent with the phase diagrams in the literature. Our simulation results suggest that strain effects play critical roles in suppressing the miscibility gap for our nanocrystalline structures whereas phase separation could occur when only the chemical miscibility gap is present. When the two phases are mixed more or less, the lattice thermal conductivity is reduced and electrical transport properties are relatively insensitive to the degree of mixing. Therefore, to maintain high thermoelectric performance, it is recommended to have strain in the lattice in order not to fall into the chemical miscibility gap. The strategy to suppress the miscibility gap bears potential impact inasmuch as many thermoelectric materials employ alloyed systems because maintaining alloying structures for low thermal conductivity could provide the stability and reliability for the actual usage of thermoelectric generators over a long period of time.

Conflicts of interest

There are no conflicts to declare.

Acknowledgements

The authors gratefully acknowledge financial support from the US National Science Foundation (Grant No. CMMI 1353156 for S. Y., C. Y., R. A.; CMMI 1462255 for V. A., R. A.; CBET 1805963 for M. J., C. Y.; and DMR 1809520 for J. J., S. X., and H. W), Texas A&M Engineering Experiment Station, and computing resources at the Terra supercomputing facility of Texas A&M University. M. J., C. Y. acknowledges financial support from the Creative Materials Discovery Program through the National Research Foundation of Korea (NRF) funded by the Ministry of Science and ICT (2018M3D1A1057844).

References

1 L.-D. Zhao, S.-H. Lo, Y. Zhang, H. Sun, G. Tan, C. Uher, C. Wolverton, V. P. Dravid and M. G. Kanatzidis, Nature, 2014, 508, 373.

- 2 S. I. Kim, K. H. Lee, H. A. Mun, H. S. Kim, S. W. Hwang, J. W. Roh, D. J. Yang, W. H. Shin, X. S. Li and Y. H. Lee, Science, 2015, 348, 109-114.
- 3 Y. Tang, Z. M. Gibbs, L. A. Agapito, G. Li, H.-S. Kim, M. buongiorno Nardelli, S. Curtarolo and G. J. Snyder, Nat. Mater., 2015, 14, 1223.
- 4 J. P. Heremans, V. Jovovic, E. S. Toberer, A. Saramat, K. Kurosaki, A. Charoenphakdee, S. Yamanaka and G. J. Snyder, Science, 2008, 321, 554-557.
- 5 A. S. Tazebay, S.-I. Yi, J. K. Lee, H. Kim, J.-H. Bahk, S. L. Kim, S.-D. Park, H. S. Lee, A. Shakouri and C. Yu, ACS Appl. Mater. Interfaces, 2016, 8, 7003-7012.
- 6 W. Liu, X. Tan, K. Yin, H. Liu, X. Tang, J. Shi, Q. Zhang and C. Uher, Phys. Rev. Lett., 2012, 108, 166601.
- 7 K. Yin, X. Su, Y. Yan, Y. You, O. Zhang, C. Uher, M. G. Kanatzidis and X. Tang, Chem. Mater., 2016, 28, 5538-5548.
- 8 W. Liu, J. Zhou, Q. Jie, Y. Li, H. S. Kim, J. Bao, G. Chen and Z. Ren, Energy Environ. Sci., 2016, 9, 530-539.
- 9 G. Polymeris, N. Vlachos, A. Khan, E. Hatzikraniotis, C. B. Lioutas, A. Delimitis, E. Pavlidou, K. Paraskevopoulos and T. Kyratsi, Acta Mater., 2015, 83, 285-293.
- 10 Q. Zhang, J. He, X. Zhao, S. Zhang, T. Zhu, H. Yin and T. Tritt, J. Phys. D: Appl. Phys., 2008, 41, 185103.
- 11 Q. Zhang, J. He, T. Zhu, S. Zhang, X. Zhao and T. Tritt, Appl. Phys. Lett., 2008, 93, 102109.
- 12 W. Liu, H. Chi, H. Sun, Q. Zhang, K. Yin, X. Tang, Q. Zhang and C. Uher, Phys. Chem. Chem. Phys., 2014, 16, 6893-6897.
- 13 P. Gao, X. Lu, I. Berkun, R. D. Schmidt, E. D. Case and T. P. Hogan, Appl. Phys. Lett., 2014, 105, 202104.
- 14 X. Liu, T. Zhu, H. Wang, L. Hu, H. Xie, G. Jiang, G. J. Snyder and X. Zhao, Adv. Energy Mater., 2013, 3, 1238-1244.
- 15 Z. Du, T. Zhu, Y. Chen, J. He, H. Gao, G. Jiang, T. M. Tritt and X. Zhao, J. Mater. Chem., 2012, 22, 6838-6844.
- 16 J.-i. Tani and H. Kido, Intermetallics, 2008, 16, 418-423.
- 17 J.-i. Tani and H. Kido, Comput. Mater. Sci., 2008, 42, 531-536.
- 18 J.-i. Tani and H. Kido, Intermetallics, 2007, 15, 1202-1207.
- 19 J.-i. Tani and H. Kido, Phys. B, 2005, 364, 218-224.
- 20 S. K. Bux, M. T. Yeung, E. S. Toberer, G. J. Snyder, R. B. Kaner and J.-P. Fleurial, J. Mater. Chem., 2011, 21, 12259-12266.
- 21 M. Akasaka, T. Iida, A. Matsumoto, K. Yamanaka, Y. Takanashi, T. Imai and N. Hamada, J. Appl. Phys., 2008, 104, 013703.
- 22 M. Akasaka, T. Iida, T. Nemoto, J. Soga, J. Sato, K. Makino, M. Fukano and Y. Takanashi, J. Cryst. Growth, 2007, 304, 196-201.
- 23 G. Nolas, D. Wang and M. Beekman, Phys. Rev. B: Condens. Matter Mater. Phys., 2007, 76, 235204.
- 24 E. K. Lee, L. Yin, Y. Lee, J. W. Lee, S. J. Lee, J. Lee, S. N. Cha, D. Whang, G. S. Hwang and K. Hippalgaonkar, Nano Lett., 2012, 12, 2918-2923.
- 25 S.-i. Yi and C. Yu, J. Appl. Phys., 2015, 117, 035105.
- 26 S. Vivès, P. Bellanger, S. Gorsse, C. Wei, Q. Zhang and J.-C. Zhao, Chem. Mater., 2014, 26, 4334-4337.
- 27 L. Yin, E. K. Lee, J. W. Lee, D. Whang, B. L. Choi and C. Yu, Appl. Phys. Lett., 2012, 101, 043114.

- 28 D. G. Rethwisch and W. D. Callister, *Materials science and engineering: an introduction*, Wiley, 9th edn, 2013.
- 29 W. Liu, X. Tang, H. Li, K. Yin, J. Sharp, X. Zhou and C. Uher, *J. Mater. Chem.*, 2012, **22**, 13653–13661.
- 30 J. W. Cahn, Acta Metall., 1961, 9, 795-801.
- 31 J. W. Cahn, Acta Metall., 1962, 10, 179-183.
- 32 F. Larché and J. W. Cahn, Acta Metall., 1985, 33, 331-357.
- 33 R. W. Balluffi, S. Allen and W. C. Carter, *Kinetics of materials*, John Wiley & Sons, 2005.
- 34 P. Voorhees and W. C. Johnson, *Solid State Phys.*, 2004, **59**, 1–201.
- 35 A. G. Khachaturyan, *Theory of structural transformations in solids*, Courier Corporation, 2013.
- 36 W. Liu, H. S. Kim, S. Chen, Q. Jie, B. Lv, M. Yao, Z. Ren, C. P. Opeil, S. Wilson and C.-W. Chu, *Proc. Natl. Acad. Sci.*, 2015, 112, 3269–3274.
- 37 A. Kozlov, J. Gröbner and R. Schmid-Fetzer, *J. Alloys Compd.*, 2011, **509**, 3326–3337.
- 38 R. Viennois, C. Colinet, P. Jund and J.-C. Tédenac, *Intermetallics*, 2012, 31, 145–151.
- 39 M. Riffel and J. Schilz, *Proceedings ICT'97, 16th International Conference on Thermoelectrics*, 1997, pp. 283–286.
- 40 P. Leo, J. Lowengrub and H.-J. Jou, *Acta Mater.*, 1998, 46, 2113–2130.
- 41 S. Hu and L. Chen, Acta Mater., 2001, 49, 1879-1890.

- 42 L. Q. Chen and J. Shen, *Comput. Phys. Commun.*, 1998, **108**, 147–158.
- 43 E. N. Nikitin, E. N. Tkalenko, V. K. Zaitsev, A. I. Zaslavskii and A. K. Kuzentsov, *Inorg. Mater.*, 1968, 4, 1656–1659.
- 44 S. F. Muntyanu, E. B. Sokolov and E. S. Makarov, *Inorg. Mater.*, 1966, 2, 740–744.
- 45 I.-H. Jung, D.-H. Kang, W.-J. Park, N. J. Kim and S. Ahn, *Calphad*, 2007, 31, 192–200.
- 46 N. Saunders and A. P. Miodownik, *CALPHAD (calculation of phase diagrams): a comprehensive guide*, Elsevier, 1998.
- 47 J. W. Gibbs, Scientific Paper, Vol1, Thermodynamics, Dover, New York, 1961.
- 48 L. Tisza, *The Thermodynamics of Phase Equilibrium*, MIT Research Laboratory of Electronics, 1960.
- 49 J. W. Cahn and F. Larché, Acta Metall., 1984, 32, 1915-1923.
- 50 J.-Y. Huh and W. Johnson, *Acta Metall. Mater.*, 1995, 43, 1631–1642.
- 51 H. Kasai, L. Song, H. L. Andersen, H. Yin and B. B. Iversen, *Acta Crystallogr., Sect. B: Struct. Sci., Cryst. Eng. Mater.*, 2017, 73, 1158–1163.
- 52 D. Zhou, J. Liu, S. Xu and P. Peng, *Comput. Mater. Sci.*, 2012, 51, 409–414.
- 53 S. Ganeshan, S. Shang, H. Zhang, Y. Wang, M. Mantina and Z. Liu, *Intermetallics*, 2009, 17, 313–318.
- 54 M. Manuel, A. Singh, M. Alderman and N. Neelameggham, *Magnesium Technology 2015*, Springer, 2016.